

Performance of Pulsed Thermal Tomography Imaging with Machine Learning-Based Classification of Defects in Additively Manufactured Structures

*Pulsed Thermal Tomography Nondestructive Examination of Additively
Manufactured Reactor Materials and Components*

Nuclear Science and Engineering Division

About Argonne National Laboratory

Argonne is a U.S. Department of Energy laboratory managed by UChicago Argonne, LLC under contract DE-AC02-06CH11357. The Laboratory's main facility is outside Chicago, at 9700 South Cass Avenue, Argonne, Illinois 60439. For information about Argonne and its pioneering science and technology programs, see www.anl.gov.

Document availability

Online Access: U.S. Department of Energy (DOE) reports produced after 1991 and a growing number of pre-1991 documents are available free at OSTI.GOV (<http://www.osti.gov/>), a service of the U.S. Dept. of Energy's Office of Scientific and Technical Information

Reports not in digital format may be purchased by the public from the National Technical Information Service (NTIS):

U.S. Department of Commerce
National Technical Information Service
5301 Shawnee Rd
Alexandria, VA 22312
www.ntis.gov
Phone: (800) 553-NTIS (6847) or (703) 605-6000
Fax: (703) 605-6900
Email: **orders@ntis.gov**

Reports not in digital format are available to DOE and DOE contractors from the Office of Scientific and Technical Information (OSTI):

U.S. Department of Energy
Office of Scientific and Technical Information
P.O. Box 62
Oak Ridge, TN 37831-0062
www.osti.gov
Phone: (865) 576-8401
Fax: (865) 576-5728
Email: **reports@osti.gov**

Disclaimer

This report was prepared as an account of work sponsored by an agency of the United States Government. Neither the United States Government nor any agency thereof, nor UChicago Argonne, LLC, nor any of their employees or officers, makes any warranty, express or implied, or assumes any legal liability or responsibility for the accuracy, completeness, or usefulness of any information, apparatus, product, or process disclosed, or represents that its use would not infringe privately owned rights. Reference herein to any specific commercial product, process, or service by trade name, trademark, manufacturer, or otherwise, does not necessarily constitute or imply its endorsement, recommendation, or favoring by the United States Government or any agency thereof. The views and opinions of document authors expressed herein do not necessarily state or reflect those of the United States Government or any agency thereof, Argonne National Laboratory, or UChicago Argonne, LLC.

Performance of Pulsed Thermal Tomography Imaging with Machine Learning-Based Classification of Defects in Additively Manufactured Structures

Pulsed Thermal Tomography Nondestructive Examination of Additively Manufactured Reactor Materials and Components

prepared by
Alexander Heifetz¹, Victoria Ankel^{1,2}, Dmitry Shribak¹, Wei-Ying Chen¹

¹Nuclear Science Engineering Division, Argonne National Laboratory

²Department of Physics, University of Chicago, Chicago, IL

September 15, 2021

Table of Contents

Table of Contents	1
List of Figures	2
Abstract	3
1. Introduction	4
2. Infrared Pulsed Thermal Tomography Imaging	5
2.1. Imaging System Setup	5
2.2. Development of Simulated Thermal Tomography Images of Metallic Plates with 2D Elliptical Defects	6
3. Convolutional Neural Network (CNN) for Classification of Thermal Tomography (TT) Images	8
3.1. Development of Convolutional Neural Network (CNN)	8
3.2. CNN Classification of Elliptical Defects in Simulated TT Images	9
3.3. CNN Classification of Defects from SEM Images of LPBF SS316 in Simulated TT Images	11
4. Conclusions	13
References	14

List of Figures

Figure 1 – Schematic drawing of infrared pulsed thermal tomography data acquisition setup.....	5
Figure 2 – Diagram demonstrating labelling of the simulated defects. Depth of the plate is along the x-axis, and y-axis is along the face of the plate. The semi-major and semi-minor axes of the elliptical air void are r_x and r_y . The ellipse is rotated by an angle θ measured relative to the y-axis.	6
Figure 3 – Simulated effusivity reconstruction of SS316 plate containing elliptical defects. (a) $r_x = 160\mu\text{m}$, $r_y = 310\mu\text{m}$, $\theta = 0^\circ$. (b) $r_x = 260\mu\text{m}$, $r_y = 310\mu\text{m}$, $\theta = 45^\circ$ (c) $r_x = 60\mu\text{m}$, $r_y = 210\mu\text{m}$, $\theta = -15^\circ$	7
Figure 4 – Flowchart of CNN algorithm.....	8
Figure 5 – Actual and predicted (classified by CNN in TT images) elliptical defects indicated by points in r_x - r_y - θ feature hyperspace diagram. Predictions are marked with squares and actual defects are marked as circles.....	9
Figure 6 – Actual elliptical defects in test TT images (green) and ellipses predicted by CNN (blue). Parameters of actual defects are (a) $r_x = 360\mu\text{m}$, $r_y = 60\mu\text{m}$, $\theta = 0^\circ$; (b) $r_x = 60\mu\text{m}$, $r_y = 310\mu\text{m}$, $\theta = 0^\circ$ (c) $r_x = 110\mu\text{m}$, $r_y = 260\mu\text{m}$, $\theta = 30^\circ$; (d) $r_x = 310\mu\text{m}$, $r_y = 160\mu\text{m}$, $\theta = -40^\circ$	10
Figure 7 – (a) SEM image of defect with equivalent ellipse dimensions $r_x = 43\mu\text{m}$, $r_y = 75\mu\text{m}$. (b) – (d) Air voids and CNN predictions with CNN (blue). Angular orientations: (b) $\theta = 37^\circ$; (c) $\theta = 43^\circ$; (d) $\theta = 8^\circ$	11
Figure 8 – (a) SEM image of defect with equivalent ellipse dimensions of $r_x = 10\mu\text{m}$ and $r_y = 37\mu\text{m}$, $\theta = 19^\circ$. (b) – (d) CNN prediction of angular orientation (blue ellipse): (b) $\theta = 18^\circ$ (c) $\theta = -42^\circ$ (d) $\theta = 1^\circ$	12

Abstract

Additive manufacturing (AM) is an emerging method for cost-efficient fabrication of complex topology nuclear reactor parts from high-strength corrosion resistance alloys, such as stainless steel and Inconel. AM of metallic structures for nuclear energy applications is currently based on laser powder bed fusion (LPBF) process. Some of the challenges with using LPBF method for nuclear manufacturing include the possibility of introducing pores into metallic structures. Integrity of AM structures needs to be evaluated nondestructively because material flaws could lead to premature failures in high temperature nuclear reactor environment. Currently, there exist limited capabilities to evaluate actual AM structures non-destructively. Pulsed Thermal Tomography Imaging (PTT) provides a capability for non-destructive evaluation (NDE) of subsurface defects in arbitrary size structures. The PTT method is based on recording material surface temperature transients with infrared (IR) camera following thermal pulse delivered on material surface with flash light. The PTT method has advantages for NDE of actual AM structures because the method involves one-sided non-contact measurements and fast processing of large sample areas captured in one image. Following initial qualification of an AM component for deployment in a nuclear reactor, a PTT system can also be used for in-service nondestructive evaluation (NDE) applications. In this report, we describe recent progress in enhancing PTT capabilities in detecting and visualizing microscopic defects in metallic specimens. The thermal tomography (TT) algorithm obtains depth reconstructions of spatial effusivity from the data cube of sequentially recorded surface temperatures. However, interpretation of TT images is non-trivial because of blurring of images with increasing depth. To address this challenge, we have developed a deep learning convolutional neural network (CNN) to classify size and orientation subsurface defects in simulated TT images. CNN is trained on a database of TT images created for a set of simulated metallic structures with elliptical subsurface voids. Test of CNN performance demonstrate the ability to classify radii and angular orientation of subsurface defects in TT images. In addition, we have shown that CNN trained on elliptical defects is capable of classifying irregular-shaped defects obtained from scanning electron microscopy (SEM) of stainless steel sections printed with LPBF.

1. Introduction

Additive manufacturing (AM) of metals is an emerging method for cost-efficient production of low volume custom structures for industries, such as nuclear energy [1]. Metals of interest for nuclear applications typically include high-strength corrosion-resistant alloys, such as stainless steel 316L (SS316L) and Inconel 718 (IN718). Because of high melting temperature, AM of SS316L and IN718 is currently based on laser powder-bed fusion (LPBF) process [2]. Due to the intrinsic features of LPBF process, pores can appear in 3D printed metallic structures [2]. With the exposure to high temperature and creep damage in high-temperature nuclear reactors, a pore can potentially become a seed for cracking [3]. Because of stringent safety requirements, each AM metallic structure needs to be qualified through nondestructive examination before deployment in a nuclear reactor [4-7]. If a defect is discovered, either a flaw mitigation with heat treatment can be performed, or the part could be disqualified from service.

Typical porosity defects observed in LPBF manufacturing consist of spheroidal-shape keyhole pores caused by excessive laser power, irregular-shape lack of fusion (LOF) pores caused by insufficient laser power, and spherical gas pores caused by trapped of gas in solidifying melt pool. Sizes of pores depend on the quality of the LPBF process. Typical sizes of keyhole and LOF pores in tens to hundreds of microns, while gas pores sizes are on the order of a few microns [5]. Prior studies indicate that larger size pores located closer to surface are more likely to cause fatigue crack initiation. High-resolution imaging with X-ray or neutron computed tomography (CT) can be used for imaging pores in small coupons to evaluate quality of LPBF process. However, applications of X-ray or neutron CT to NDE of actual AM structures are limited because of large size, lack of symmetry and complex shapes of AM structures. Ultrasonic testing is scalable with structure size, but face challenges because the rough surfaces, characteristic of AM structures, affect the probe coupling. For high-resolution ultrasonic tomography, imaging of large structures is time-consuming because of point-by-point raster scanning of specimens.

We investigate Infrared Pulsed Thermal Tomography (PTT) for detection of subsurface microscopic pores in AM structures. This method offers several potential advantages because PTT measurements are one-sided, non-contact, and scalable to arbitrary size structures [8-10]. The PTT method consists of recording material surface temperature transients with an infrared (IR) camera, following deposition of thermal impulse on material surface with a flash lamp. Thermal tomography (TT) algorithm obtains depth reconstructions of spatial effusivity from the data cube of sequentially recorded surface temperatures. However, interpretation of TT images is non-trivial because of blurring of images with increasing depth. In this report, we describe development of a deep learning convolutional neural network (CNN) to classify size and orientation subsurface defects in simulated thermal tomography (TT) images [11]. CNN is trained on a database of TT images created for a set of simulated metallic structures with elliptical subsurface voids. Test of CNN performance demonstrate the ability to classify radii and angular orientation of subsurface defects in TT images. In addition, we show that CNN trained on elliptical defects is capable of classifying irregular-shaped defects obtained from scanning electron microscopy (SEM) of stainless steel sections printed with LPBF.

2. Infrared Pulsed Thermal Tomography Imaging

2.1. Imaging System Setup

In the experimental PTT system, data is acquired with a laboratory setup consisting of a megapixel fast frame infrared (IR) camera and flash lamp is shown in schematic depiction in Figure 1. A pulse trigger sends a signal to capacitor to discharge in a circuit containing white light flash lamp. The flash lamp source delivers a pulse of thermal energy to material surface. Heat transfer takes place from the heated surface to the interior of the sample, resulting in a continuous decrease of the surface temperature. For better heat absorption, and to remove the effect of different surface emissivity, all materials in this study were spray-painted with washable graphite paint. As heat deposited with flash lamp the surface starts diffusing into the material bulk, presence of low-density internal material inclusions is revealed through appearance of local temperature “hot spots” on the surface. This effect occurs because low density defects have lower thermal diffusivity compared with solid material. The defects act as thermal resistances and slow down thermal diffusion, which causes temperature difference on the material surface between regions of defects and non-defects. A megapixel fast frame infrared (IR) camera records blackbody radiation to obtain time-resolved images of surface temperature distribution $T(x,y,t)$. The acquired thermal-imaging data cube therefore consist of a series of 2D images of the sample’s surface temperature at consecutive time instants. Thermal tomography algorithms performs reconstruction of spatial effusivity $e(x,y,z)$, which allows for depth visualization of material defects.

The laboratory system for data acquisition uses a FLIR x8501sc with Indium Antimonide (InSb) detector camera, which has integration time of 270ns, NETD sensitivity of $<30\text{mK}$, and frame rate of at 180Hz at full frame imaging. The flash lamp source (Balcar ASYM 6400 in the experiment) delivers a pulse of 6400J/2ms thermal energy to material surface. The flash lamp is typically positioned at 30cm to 50cm distance to the specimen under investigation. The exact distance and angle of illumination of the flash lamp are determined experimentally for each specimen. This is decided by positioning the IR camera at the focal length of the lens, and placing the flash lamp such that the IR field of view is not blocked, nor does IR camera block the flash.

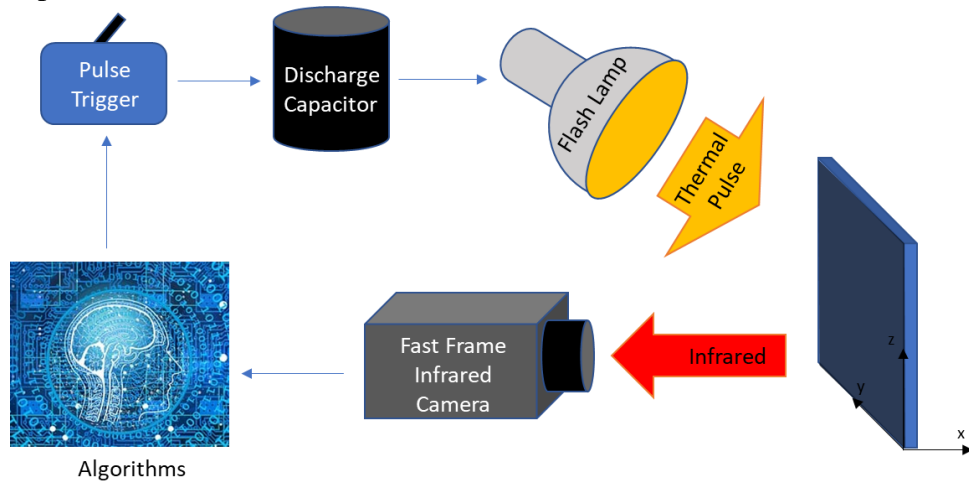


Figure 1 – Schematic drawing of infrared pulsed thermal tomography data acquisition setup

2.2. Development of Simulated Thermal Tomography Images of Metallic Plates with 2D Elliptical Defects

In this work, we model defects in AM steel as elliptical air voids in 2D. We choose to use an elliptical model for the defect because thermal imaging based on heat diffusion smooths out rough edges present in the defect. This smoothing effect means that an arbitrarily shaped defect can be potentially described with an equivalent ellipse. The diagram depicting elliptical void labeling is given in Figure 2. The x-axis is along the depth of the plate, and the y-axis is along the face of the plate. The ellipse is characterized by semi-major and semi-minor axes r_x and r_y , and angular orientation θ measured from the y-axis. PTT system performance for SS316 plates with elliptical defects was simulated with 2D heat transfer using MATLAB PDE Toolbox.

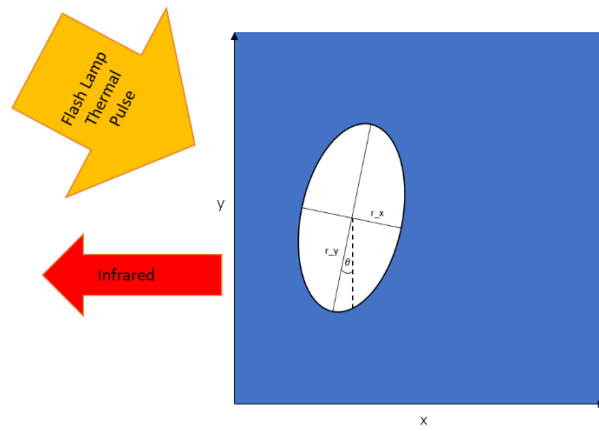


Figure 2 – Diagram demonstrating labelling of the simulated defects. Depth of the plate is along the x-axis, and y-axis is along the face of the plate. The semi-major and semi-minor axes of the elliptical air void are r_x and r_y . The ellipse is rotated by an angle θ measured relative to the y-axis.

Simulated effusivity reconstructions $e(x,y)$ were obtained for surface temperature transients generated with MATLAB heat transfer computer simulations for SS316 plates containing elliptical voids with different sizes and orientations by simulating. Thermal tomography (TT) reconstruction algorithm calculates spatial effusivity from the data cube of surface temperature measurements to visualize internal material defects. Depth profile of effusivity $e(x)$ is obtained from surface temperature measurements as follows

$$e(x) = x \frac{2Q}{\pi\sqrt{\alpha}} \frac{d}{dt} \left(\frac{1}{T(t)} \right) \bigg|_{t=x^2/\pi\alpha} \quad (1)$$

where Q is the instantaneously deposited surface thermal energy density, and α is the uniform material thermal diffusivity [11,12]. Three examples of effusivity reconstruction of SS316 plates with dimensions 5mm x 5mm containing defects ($r_x = 160\mu\text{m}$, $r_y = 310\mu\text{m}$ and $\theta = 0^\circ$), ($r_x = 260\mu\text{m}$,

$r_y = 310\mu\text{m}$, and $\theta = 45^\circ$), and ($r_x = 60\mu\text{m}$, $r_y = 210\mu\text{m}$ and $\theta = -15^\circ$) are shown below in Figures 3(a), 3(b) and 3(c), respectively. Reconstructions were performed for assumed imaging frame rate of 540Hz and 340 pixels spatial sampling of 5mm-long surface line.

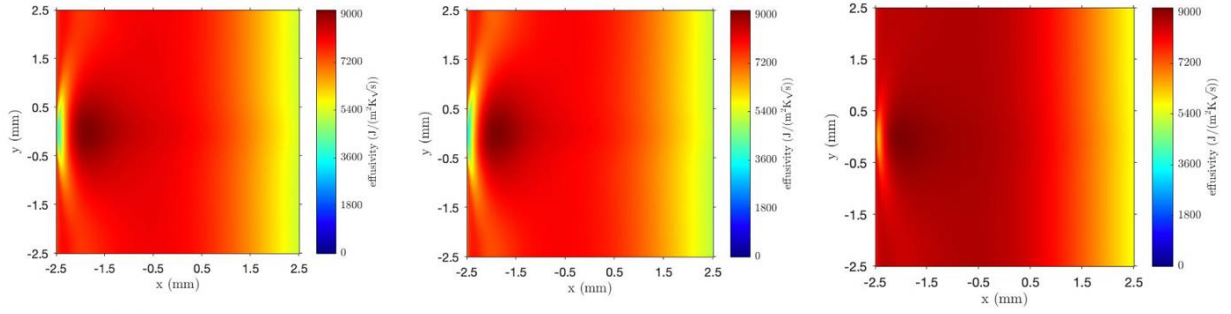


Figure 3 – Simulated effusivity reconstruction of SS316 plate containing elliptical defects. (a) $r_x = 160\mu\text{m}$, $r_y = 310\mu\text{m}$, $\theta = 0^\circ$. (b) $r_x = 260\mu\text{m}$, $r_y = 310\mu\text{m}$, $\theta = 45^\circ$ (c) $r_x = 60\mu\text{m}$, $r_y = 210\mu\text{m}$, $\theta = -15^\circ$

3. Convolutional Neural Network (CNN) for Classification of Thermal Tomography (TT) Images

3.1. Development of Convolutional Neural Network (CNN)

We developed a deep learning convolutional neural network (CNN) for classification of defects in effusivity reconstruction images. The CNN takes effusivity reconstruction images as inputs, and returns characteristic dimensions r_x , r_y , and θ of the elliptical defects. The flow chart of CNN algorithm is shown in Figure 4. To construct the CNN, we used AutoKeras's image classification class. There are four layers to the CNN: The input node is ImageInput, specific to images as represented by a Python numpy array. The training and test images in the input layer of CNN are of the same size. Following the input node, the CNN uses two AutoKeras blocks—ConvBlock and DenseBlock. AutoKeras is unique in that arguments are tuned automatically, and therefore left initially unspecified. ConvBlock includes convolutional and pooling layers required for the CNN, and DenseBlock encompasses the fully connected network following the convolutional layers. In the CNN process, convolution layers are followed by pooling layers, until a flattening layer compresses the data into a one-dimensional array. Convolution layers consists of identical neurons that are connected to local neurons in previous layer. As the neuron, or filter, operates on parts of the input image, its pixel values are multiplied by the filter values. This convolution operation creates a “feature map” from the original image. This allows features of the image to be isolated and identified. More convolution layers allow the CNN to detect lower-level features within the image, which is why convolution layers are usually stacked. Pooling layers—in this case max pooling layers—are also utilized between convolution layers to keep feature maps generalized. Max pooling takes the maximum value from each segment of the feature map produced by a given convolutional layer. Thus, pooling is necessary to ensure that the CNN is sensitive to small translations in the input. After flattening, this array is passed through a traditional fully connected (dense) layer to make the final prediction.

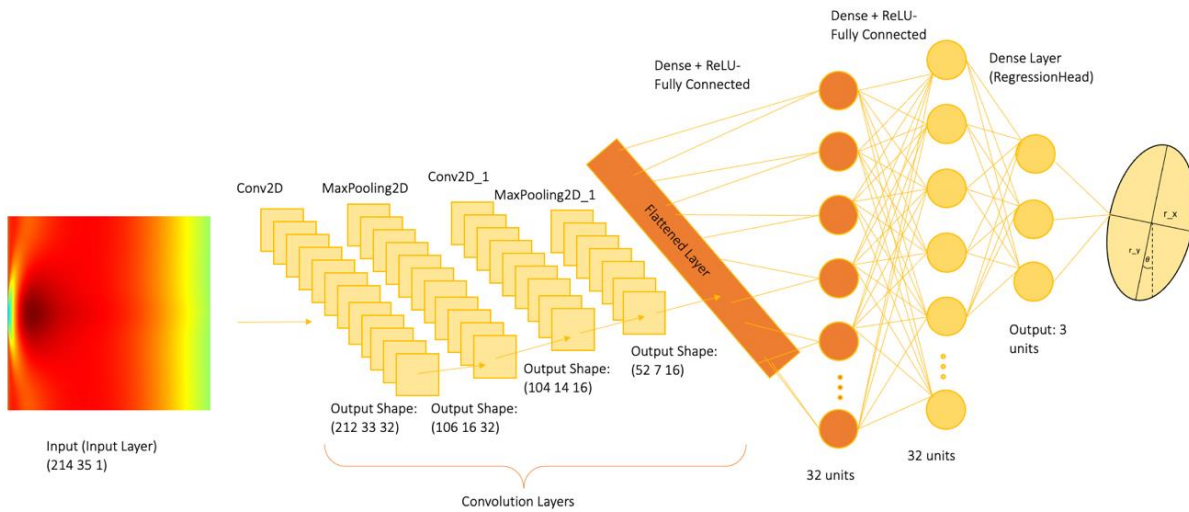


Figure 4 – Flowchart of CNN algorithm

A CNN has some advantages over a fully connected network, especially in image analysis and classification. The CNN's feature map makes it particularly adept at detecting the subtle features important aspects of images, crucial for image classification. Additionally, CNN uses copies of the same neuron to process data, which saves both time and memory. As a result, training and prediction computer running time of the CNN is less than 150 seconds on average.

3.2. CNN Classification of Elliptical Defects in Simulated TT Images

The training set for CNN consisted of 100 simulated thermal effusivity images for plates with elliptical defects with different sizes and angular orientations. The defects range in size from $20 \times 20 \mu\text{m}$ to $310 \times 310 \mu\text{m}$ with angular orientations in the range from -45° to 45° . The test set consisted of 15 different images, which were not part of the training set. Performance of CNN in classification of defects in 10 TT images in the test set is illustrated in Figure 5. Characteristic dimensions of defects are displayed as points in r_x - r_y - θ feature hyperspace diagram. Actual defects are indicated with circles, and predictions with CNN are indicated with squares. Qualitatively, the error in CNN predictions is quite small.

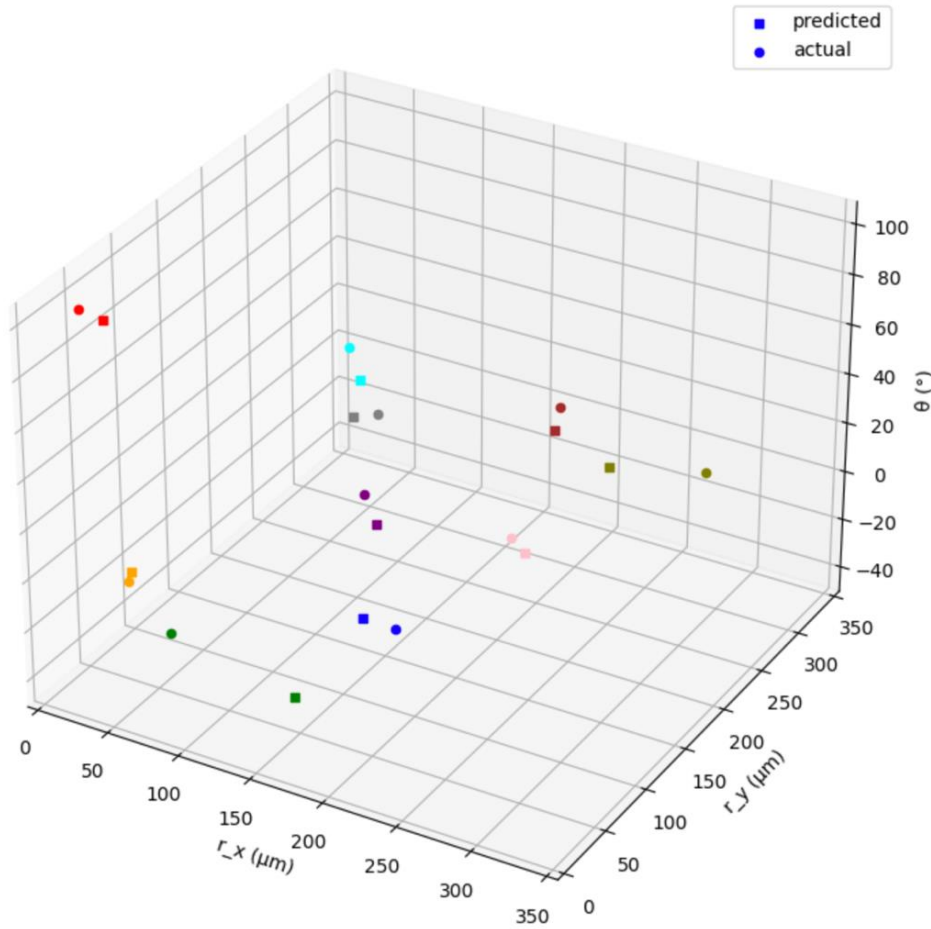


Figure 5 – Actual and predicted (classified by CNN in TT images) elliptical defects indicated by points in r_x - r_y - θ feature hyperspace diagram. Predictions are marked with squares and actual defects are marked as circles

Figure 6 illustrates CNN performance in classification of elliptical defects in simulated TT images by displaying on the same set of axis ellipses corresponding to actual and predicted set of r_x , r_y , and θ values. The actual defects in test TT images are drawn with green color. Ellipses predicted with CNN are shown in blue. Parameters of the four actual elliptical defects shown in Figures 6(a) through 6(d) are ($r_x = 360\mu\text{m}$, $r_y = 60\mu\text{m}$, $\theta = 0^\circ$), ($r_x = 60\mu\text{m}$, $r_y = 310\mu\text{m}$, $\theta = 0^\circ$), ($r_x = 110\mu\text{m}$, $r_y = 260\mu\text{m}$, $\theta = 30^\circ$), ($r_x = 310\mu\text{m}$, $r_y = 160\mu\text{m}$, $\theta = -40^\circ$). Qualitatively, predictions obtained with CNN have a relatively small error.

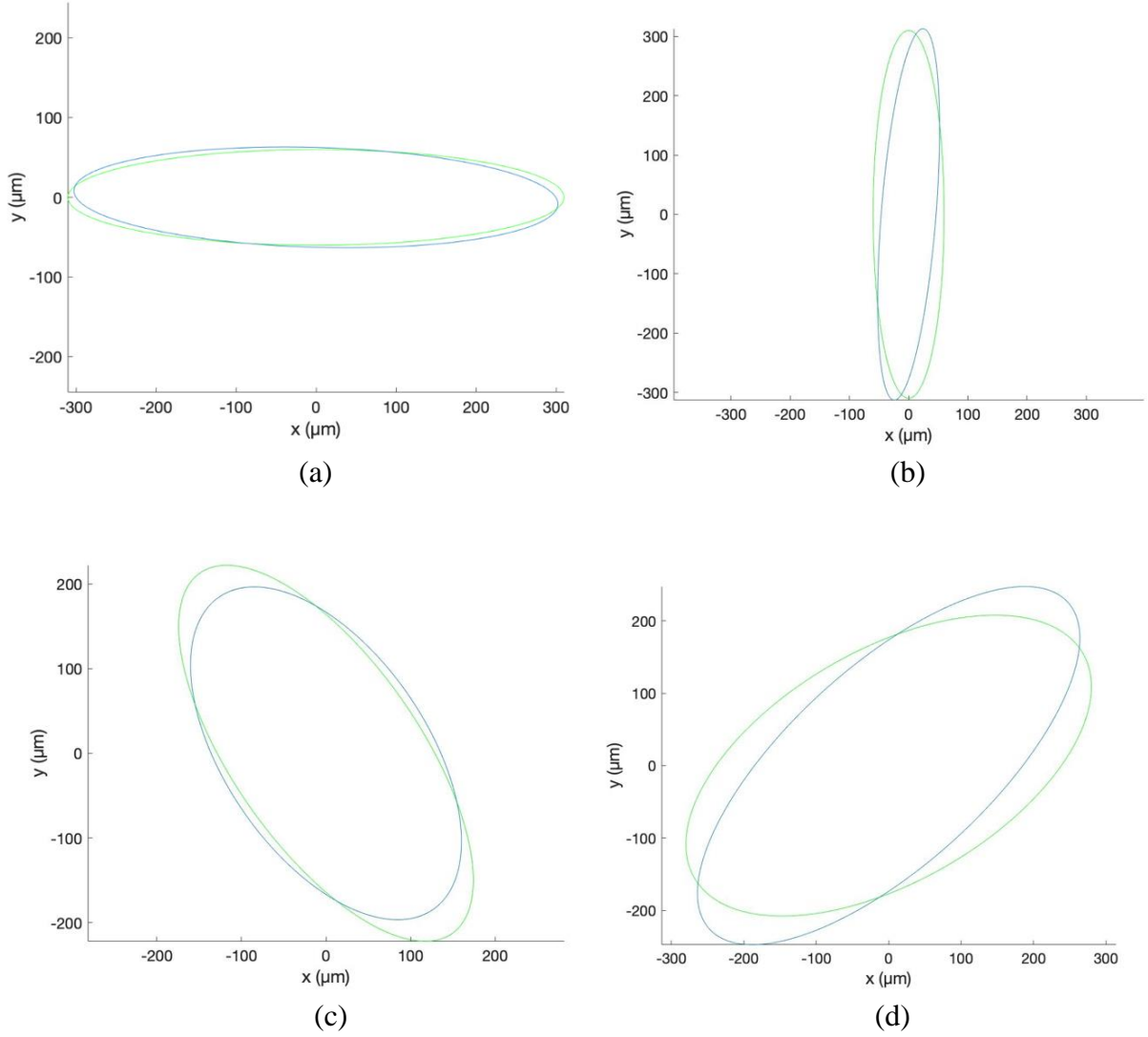


Figure 6 – Actual elliptical defects in test TT images (green) and ellipses predicted by CNN (blue). Parameters of actual defects are (a) $r_x = 360\mu\text{m}$, $r_y = 60\mu\text{m}$, $\theta = 0^\circ$; (b) $r_x = 60\mu\text{m}$, $r_y = 310\mu\text{m}$, $\theta = 0^\circ$ (c) $r_x = 110\mu\text{m}$, $r_y = 260\mu\text{m}$, $\theta = 30^\circ$; (d) $r_x = 310\mu\text{m}$, $r_y = 160\mu\text{m}$, $\theta = -40^\circ$

3.3. CNN Classification of Defects from SEM Images of LPBF SS316 in Simulated TT Images

We investigate if CNN trained on TT images with elliptical defects is capable of classifying irregular shape defects. For this study, we use SEM (scanning electron microscopy) images of actual defects in LPBF SS316 specimens. One example of such defect is shown in Figure 7(a). To characterize this defect we extract the shape from the SEM image and fit an ellipse with an equivalent surface area. For the defect in Figure 7(a), we estimate that $r_x = 43\mu\text{m}$, $r_y = 75\mu\text{m}$, and $\theta = 37^\circ$. The air voids with the shape extracted from the SEM image are shown in Figures 7(b) to 7(d). Angular orientations are $\theta = 37^\circ$, $\theta = 53^\circ$ and $\theta = 8^\circ$, respectively. TT images were developed by creating plate structures with embedded air voids with the shapes of the defects shown in Figures 7(b) to 7(d), performing heat transfer calculations with MATLAB, and calculating thermal effusivity reconstructions. CNN predictions are shown in Figures 7(b) to 7(d) with blue ellipses.

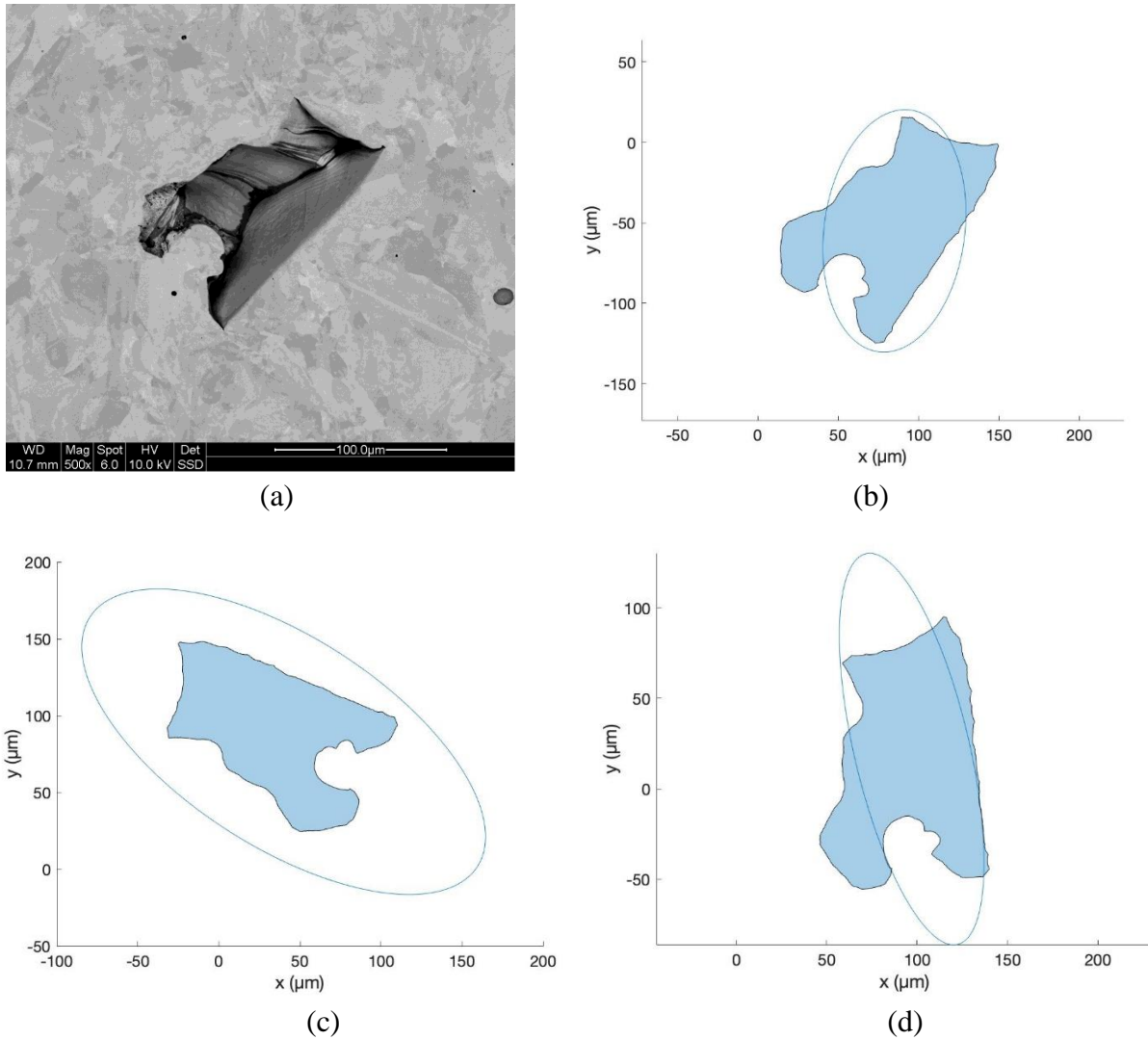


Figure 7 – (a) SEM image of defect with equivalent ellipse dimensions $r_x = 43\mu\text{m}$, $r_y = 75\mu\text{m}$. (b) – (d) Air voids and CNN predictions with CNN (blue). Angular orientations: (b) $\theta = 37^\circ$; (c) $\theta = 43^\circ$; (d) $\theta = 8^\circ$

Another defect in LPBF SS316 imaged with SEM is shown in Figure 8(a). We following the same procedure of extracting the shape from SEM image, and fitting an equivalent area ellipse. The size of the equivalent ellipse for the defect in Figure 8(a) is $r_x = 10\mu\text{m}$ and $r_y = 37\mu\text{m}$, with $\theta = 19^\circ$ orientation. Figures 8(b) to 8(d) show CNN predictions (blue ellipses) for TT images with embedded rotated air void. Angular orientations of ellipses CNN associates with the defects in Figures 8(b) to 8(d) are $\theta = 18^\circ$, $\theta = -42^\circ$ and $\theta = 1^\circ$. Qualitatively, the error in CNN predictions is relatively small.

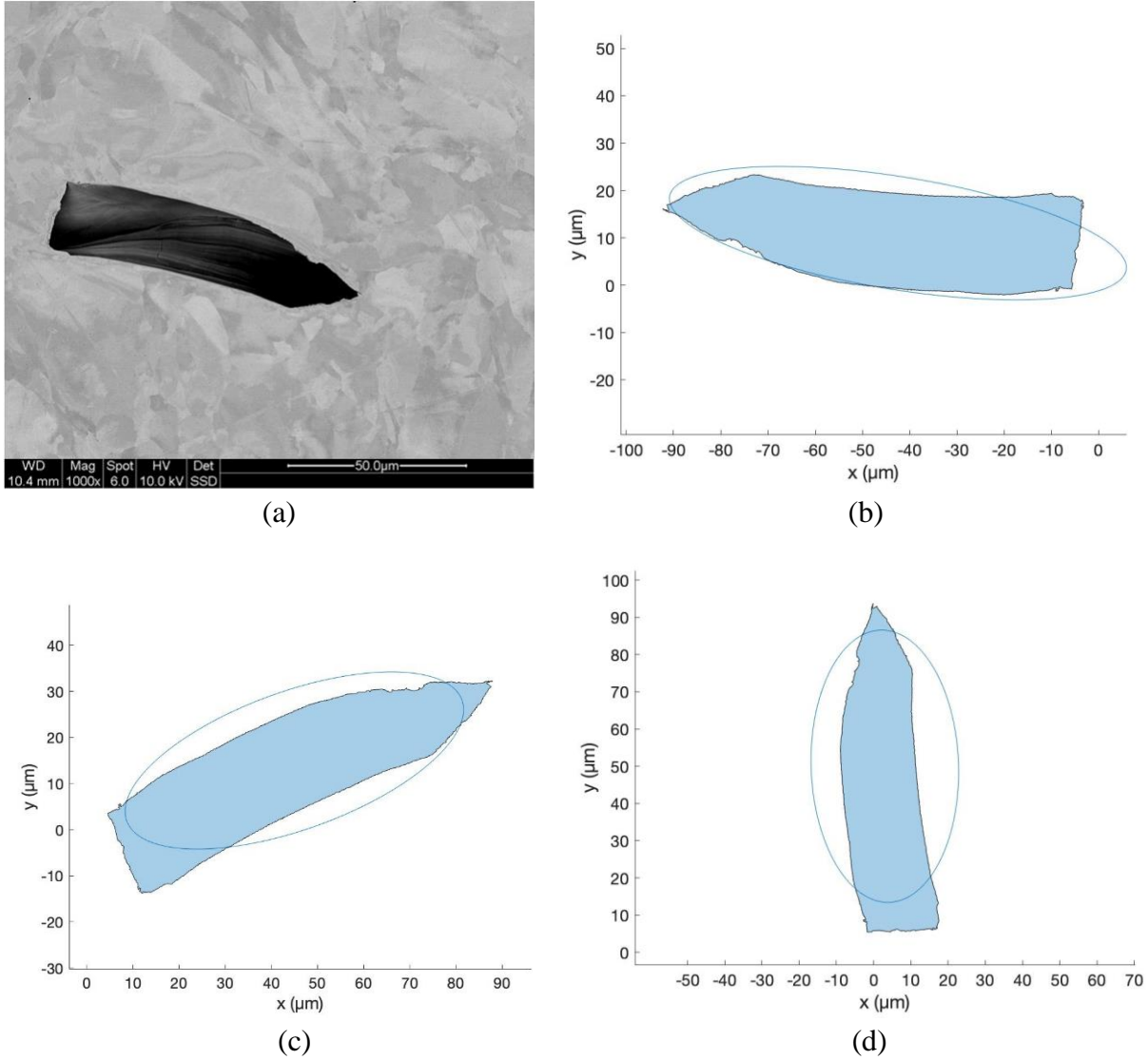


Figure 8 – (a) SEM image of defect with equivalent ellipse dimensions of $r_x = 10\mu\text{m}$ and $r_y = 37\mu\text{m}$, $\theta = 19^\circ$. (b) – (d) CNN prediction of angular orientation (blue ellipse): (b) $\theta = 18^\circ$ (c) $\theta = -42^\circ$ (d) $\theta = 1^\circ$

4. Conclusions

We have described development of a deep learning convolutional neural network (CNN) to classify size and orientation subsurface defects in simulated thermal tomography (TT) images. CNN is trained on a database of TT images created for a set of simulated metallic structures with elliptical subsurface voids. TT images were created with MATLAB PDE Toolbox heat transfer calculations for 2D structures. Test of CNN performance demonstrate the ability to classify radii and angular orientation of subsurface defects in TT images. In addition, we have shown that CNN trained on elliptical defects is capable of classifying irregular-shaped defects obtained from scanning electron microscopy (SEM) of stainless steel sections printed with LPBF.

In future developments, we plan extend our method to the classification of 3D defects. This can be accomplished by calculating heat transfer in 3D for a structure containing an internal defect. The CNN can be modified to take 3D arrays as an input and perform classification of 3D defect shapes. In addition, in both 2D and 3D models, we can test CNN in detecting of cracks in TT images. Good performance of CNN classification of ellipses elongated in the direction perpendicular to the plate surface gives an indication that crack detection using this computational technique is possible.

References

1. X. Lou and D. Gandy, "Advanced Manufacturing for Nuclear Energy," JOM 71, 2834-2836 (2019).
2. S. A. Khairallah, A. T. Anderson, A. Rubenchik, W. E. King, "Laser Powder-Bed Fusion Additive Manufacturing: Physics of Complex Melt Flow and Formation Mechanisms of Pores, Spatter and Denudation Zones," Acta Materialia 108, 36-45 (2016).
3. M. D. Sangid, P. Ravi, V. Prithvirajan, N. A. Miller, P. Kenesei, J.-S. Park, "ICME Approach to Determining Critical Pore Size of IN718 Produced by Selective Laser Melting," JOM 72, 465-474 (2019).
4. X. Zhang, J. Saniie, W. Cleary, A. Heifetz. (2020). "Quality Control of Additively Manufactured Metallic Structures with Machine Learning of Thermography Images," JOM 72(12), 4682-4694 (2020).
5. X. Zhang, J. Saniie, A. Heifetz, "Detection of Defects in Additively Manufactured Stainless Steel 316L with Compact Infrared Camera and Machine Learning Algorithms," JOM 72(12), 4244-4253 (2020).
6. X. Zhang, J. Saniie, A. Heifetz, "Neural Learning Based Blind Source Separation for Detection of Material Defects in Pulsed Thermography Images," Proceedings of 2020 IEEE International Conference on Electro-Information Technology (EIT), 112-116 (2020).
7. X. Zhang, J. Saniie, A. Heifetz, "Spatial Temporal Denoised Thermal Source Separation in Images of Compact Pulsed Thermography System for Qualification of Additively Manufactured Metals," Proceedings of 2021 IEEE International Conference on Electro-Information Technology (EIT), 209-214 (2021).
8. A. Heifetz, D. Shribak, X. Zhang, J. Saniie, Z.L. Fisher, T. Liu, J.G. Sun, T. Elmer, S. Bakhtiari, W. Cleary, "Thermal Tomography 3D Imaging of Additively Manufactured Metallic Structures," AIP Advances 10(10), 105318 (2020).
9. A. Heifetz, J.G. Sun, D. Shribak, T. Liu, T.W. Elmer, P. Kozak, S. Bakhtiari, B. Khaykovich, W. Cleary, "Pulsed Thermal Tomography Nondestructive Evaluation of Additively Manufactured Reactor Structural Materials," Transactions of the American Nuclear Society 121(1), 589-591 (2019).
10. A. Heifetz, D. Shribak, Z.L. Fisher, W. Cleary, "Detection of Defects in Additively Manufactured Metals Using Thermal Tomography," TMS 2021 150th Annual Meeting & Exhibition Supplemental Proceedings, 121-127 (2021).
11. V. Ankel, D. Shribak, A. Heifetz, "Defect Classification in Simulated Pulsed Thermal Tomography Images using Deep Learning Convolutional Neural Network," accepted at ANS Winter Meeting 2021.



Nuclear Science and Engineering (NSE) Division

Argonne National Laboratory

9700 South Cass Avenue, Bldg. 208

Argonne, IL 60439

www.anl.gov



Argonne National Laboratory is a U.S. Department of Energy
laboratory managed by UChicago Argonne, LLC